RESEARCH ARTICLE

ADVANCED ENGINEERING MATERIALS

www.aem-journal.com

Hyper-Elastic Deformation via Martensitic Phase Transformation in Cadmium Telluride

Kun Luo, Xiao Han, Jonathan Cappola, Dian Li, Yufeng Zheng, Lin Li, Feng Yan,* and Qi An**

Cadmium telluride (CdTe) is a highly promising material for photovoltaics (PV) and photodetectors due to its light-absorbing properties. However, efficient design and use of flexible devices require a deep understanding of its atomic-level deformation mechanism. Herein, uniaxial compression deformation of CdTe monocrystalline with varying crystal orientations is investigated using molecular dynamics (MD) with a newly developed machine-learning force field (ML-FF), alongside in-situ micropillar compression experiments. The findings reveal that CdTe bulk deformation is dominated by reversible martensitic phase transformation, whereas CdTe pillar deformation is primarily driven by dislocation nucleation and movement. CdTe monocrystals possess exceptional super-recoverable deformation along the $<100>$ orientation due to hyper-elastic processes induced by martensitic transformation. This discovery not only sheds light on the peculiarities observed in micropillar experimental measurements, but also provides pivotal insights into the fundamental deformation behaviors of CdTe and similar II–VI compounds under various stress conditions. These insights are crucial for the innovative design and enhanced functionality of future flexible electronic devices.

1. Introduction

Flexible photovoltaic (PV) devices, i.e., solar cells, offer an affordable, scalable, and sustainable way to convert solar energy into electrical energy.[1] Cadmium telluride (CdTe) with zinc-blende structure is successfully used in thin-film solar cells technology, due to its high power conversion efficiency, low cost, and lightweight properties.[2–4] However, CdTe based solar cells are typically manufactured on a glass substrate, which can make them heavy and fragile. In contrast, solar cells on a flexible substrate are lightweight, can deform, and are suitable for use in flexible PV devices for both space and terrestrial applications. It is well known that conventional mechanical failure, such as cracks, fractures, and bending, can damage solar panels and other devices. Flexible PV devices require PV materials with a more robust capability to safely deform than a high conversion efficiency. Therefore, it is essential to understand the deformation and failure mechanisms of CdTe to develop flexible PV devices with different shapes and deformation capabilities, such as safe curvature and strain range.

The mechanical behavior of CdTe has been explored in previous studies by evaluating the effects of stress on the formation and multiplication of dislocations during the directional solidification at temperatures ranging from 100 K to near its melting point of 1355 K.[5,6] However, these studies were limited to observing the stress–strain behavior of [132] oriented monocrystalline at different temperatures, yet dislocation motion was not observed under the experimental conditions. Other investigations of dislocation motion at room temperature in CdTe monocrystals revealed that while the Peierls mechanism controls the short-range dislocation motion, the multiplication rate and the mean free path of dislocations govern the macroscopic strain-rate.[7] Subsequent studies focused on the effects of dislocations on the electrical and optical properties of CdTe.[8–10] These studies used indentation experiments to plastically deform CdTe and produce dislocation loops and other defects. However, these experiments were not designed to investigate the deformation mechanisms of CdTe crystals.

Studying the deformation mechanism of materials, especially regarding nano defects and structural changes, poses significant challenges for experimental methods alone. Theoretical simulations can help overcome the limitations of the existing experimental techniques to a certain extent. Molecular dynamics (MD) technique is a highly effective method for simulating the mechanical behavior of materials at an atomic level under various

K. Luo, Q. An
Department of Materials Science and Engineering
Iowa State University
Ames, IA 50011, USA
E-mail: qan@iastate.edu

X. Han, J. Cappola, L. Li, F. Yan
Department of Metallurgical and Materials Engineering
The University of Alabama
Tuscaloosa, AL 35487, USA
E-mail: lin.li.10@asu.edu; fengyan@asu.edu

J. Cappola, L. Li, F. Yan
School for Engineering of Matter, Transport and Energy
Arizona State University
Tempe, AZ 85287, USA

D. Li, Y. Zheng
Department of Materials Science and Engineering
University of North Texas
Denton, TX 76203, USA

The ORCID identification number(s) for the author(s) of this article can be found under https://doi.org/10.1002/adem.202302076.

DOI: 10.1002/adem.202302076

loadings.[11,12] For instance, Zhang et al. utilized MD simulations to investigate the mechanical properties of nanotwinned CdTe under nanoindentation, exploring the relationship between hardness and twin boundaries.[13–15] Similarly, the deformation mechanism of the nanotwinned CdTe under nanoindentation and the effect of twin boundaries on the mechanical properties were investigated at an atomic level using MD simulations.[16] MD simulations have also been applied to investigate the mechanical behavior of CdTe nanowires (NWs) under varying conditions such as size, temperature, crystal orientation, and strain rate during both tension and compression.[17] However, there is limited research on the deformation mechanism of CdTe monocrystalline bulk using MD simulations, and the classical interatomic potential utilized in such simulations can significantly affect the results obtained.[17,18]

Machine-learning force fields (ML-FFs) trained from density functional theory (DFT) calculations have recently garnered increased attention for their computational efficiency and DFT-level accuracy. The use of ML-FFs greatly expands the scope of MD simulations and has been applied in various research fields, including organic molecules,[19] low-dimensional materials,[20] metals,[21] and semiconductors.[22] Herein, we investigate the mechanical responses of CdTe single crystals along different orientations by combining mechanical experiments and MD simulations. Our selection of the <100>, <110>, and <111> orientations is rooted in their distinct surface properties and relevance in semiconductor applications. The polar nature of CdTe (100) and CdTe (111) and the zigzag geometry of the non-polar (110) direction significantly influence the material's mechanical and functional behavior, particularly in photoconductive and photovoltaic devices.[23] This choice enhances our understanding of CdTe's mechanical behavior in different crystal orientations, pivotal for future flexible device applications. Furthermore, to replicate ideal conditions for single crystal studies and to delve into their intrinsic mechanisms, we utilized an in-situ scanning electron microscopy (SEM)-based micro-compression test. This technique facilitates a precise observation and analysis of deformation behaviors under near-natural conditions of the single crystals, offering deeper insights into their fundamental mechanisms. Owing to MD simulations with accurate ML-FF, we discover that the distinctive deformation behavior observed in mechanical experiments along the <100> direction is attributable to hyperelastic deformation, a result of reversible martensitic transformation. This transformation follows the classical face-centered cubic (FCC) to body-centered cubic (BCC) phase transition pathway. Through MD simulations, we have comprehensively characterized this process, detailing the nucleation and subsequent growth phases of the transformation. This research illuminates the complex deformation mechanisms of CdTe under diverse loading conditions, laying the groundwork for the development and optimization of more efficient and versatile flexible devices.

2. Results and Discussion

2.1. Experimental Measured Mechanical Responses of Single Crystal CdTe along Different Orientations

Firstly, the mechanical responses of high-quality single crystals along <100>, <110>, and <111> directions (**Figure 1**a) were evaluated using an in-situ SEM compression test. The mechanical behaviors of single-crystal CdTe along the <100>, <110>, and <111> orientations were explored through macroscopic nanoindentation (Figure 1e) and in-situ SEM micro-pillar compression tests (Figure 1f). The nanoindentation measurements revealed that single-crystal CdTe exhibits an average hardness of approximately 755, 813, and 751 MPa along the <100>, <110>, and <111> directions, respectively. Furthermore, the recovery curves yielded Young's moduli of 22.5, 29.2, and 32.0 GPa for these respective directions. Notably, the <100> direction showed a greater deviation from linear elastic recovery, markedly different from the elastic recovery processes of the other two orientations (Figure 1e). Figure 1f compares the stress–strain responses of micro-pillars oriented in the three directions, subjected to in-situ compression tests at a constant strain rate of $2 \times 10^{-3}\,\mathrm{s}^{-1}$. The yield strengths measured for the micro-pillars oriented along <100>, <110>, and <111> directions were 197, 315, and 385 MPa, respectively. Notably, the <111> directions, while having the lowest hardness, exhibited the highest compressive strength compared to the other two directions. This finding is in alignment with previously reported simulation results for CdTe,[24] and it also correlates with experimental results observed in single diamond with similar structures.[25] Upon yielding, the <110> and <111> oriented pillars deformed with a similar strain hardening rate, which was higher than that of the <100> orientation. Meanwhile, the <100> oriented pillar exhibited a lower hardening rate initially, with an extended plateau up to 5%. Subsequently, the strain hardening rate gradually increased with further straining up to 20%. This two-stage deformation trend was also distinctly different from the other two orientations. The results from these two different testing methods consistently indicate that the deformation behavior of the <100> orientation is unique compared to the other two directions. This is unlikely to be a coincidence and suggests that the <100> direction possesses a distinctive deformation mechanism, necessitating further investigation through MD studies.

2.2. Deformation Mechanism along <100>-Oriented CdTe Bulk

Three simulation models mimicking <100>, <110>, and <111>-oriented CdTe monocrystalline were constructed with dimensions of 7.8–8.0, 7.8–7.9, and 13.0–13.6 nm along x, y, z directions, respectively, as shown in Figure 1b. Figure 1c gives the corresponding pillar model. The simulation models contain about 18,000 atoms. The evolution of stress, structure, and dislocation during the compression deformation of the <100>-oriented CdTe bulk is shown in **Figure 2**. The stress–strain curve in Figure 2a shows that the compression process consists of five stages: 1) an initial linear response stage within the strain of 7%; 2) a continuous but nonlinear response stage within the strain between 7% and 26%; 3) another linear response stage within the strain between 26% and 34%; 4) a continuous but nonlinear response stage within the strain between 34% and 36%; and 5) a load drop stage, i.e., failure stage, with strain beyond 36%. The evolution of phase content was almost synchronous with the stress–strain curve during compression loading, while dislocations only appeared at the final failure stage with strain beyond

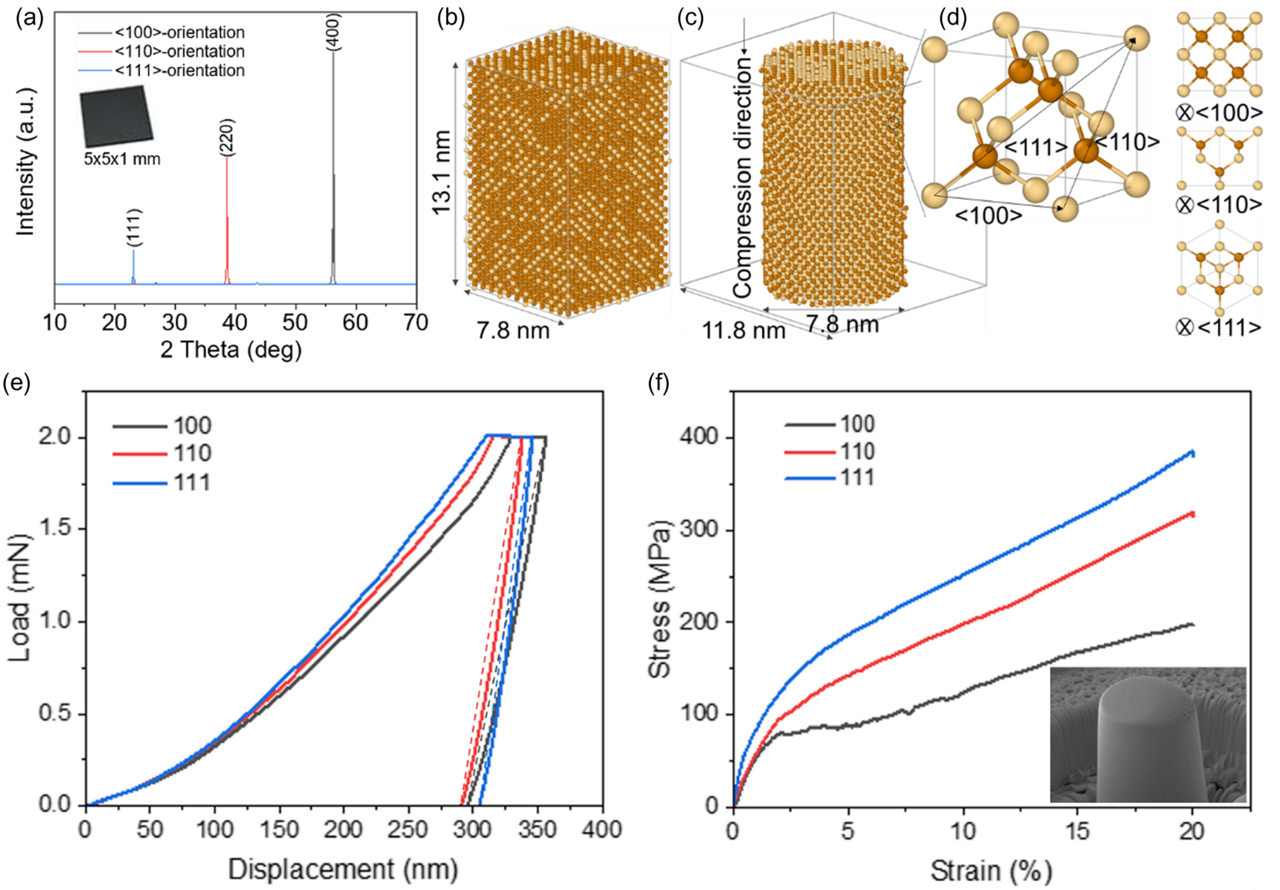

Figure 1. Structural information and mechanical behavior of the single-crystal CdTe orientated along <100>, <110>, and <111> directions: a) XRD spectra for the CdTe single crystal in different orientations; the inset displays the bulk morphology of the raw CdTe single crystal. b) Bulk model; c) pillar model; d) unit cell showing the ZB-CdTe in different orientations. Cd and Te atoms are represented by light yellow and brown balls, respectively. e) Nanoindentation loading/unloading curves; the elastic recovery curve for the <100> direction shows a more pronounced deviation from the ideal linear recovery curve (dashed line). f) In-situ micropillar compression curves; the inset displays the approximately 10.5 μm diameter nanopillars used in the experiments. Notably, the curve corresponding to the <100> direction exhibits deformation behavior distinctly different from the other two orientations.

36%. This indicates a dominant and competitive relationship between these two atomic mechanisms at different stages during the compression deformation of the <100>-oriented CdTe bulk (Figure 2a–c). The overlapping of the loading and unloading curves within a strain of 36% indicates that the nonlinear response stage can be attributed to this hyper-elastic deformation. This might explain the unique deformation behavior observed in the <100> direction in the aforementioned experiments. This phenomenon is common in shape memory alloys and is caused by reversible martensitic transformation.[26] Therefore, we found a martensitic transformation from ZB-CdTe into a *β*-tin-like structure during the hyper-elastic deformation, as shown in Figure 2d. The *β*-tin-like structure is the intermediate phase of martensitic transformation from ZB-CdTe to *β*-tin CdTe,[27] which also has a space group of *I*-4 *m*2 but with a larger *c*/*a* value. Since OVITO cannot recognize this complex structure, we analyze the phase transformation of Cd-sublattice in CdTe that OVITO can recognize. Thus, the correspondence is as follows: FCC-Cd corresponds to ZB-CdTe with zinc-blende structure; Hexagonal close-packed (HCP)-Cd corresponds to WZ-CdTe with wurtzite structure; and BCC-Cd corresponds to the newly discovered β-tin-like structure. Therefore, for subsequent analysis convenience, the phase transformation of CdTe presented here is simplified into the typical martensitic transformation from FCC to BCC.

We analyze the deformation mechanism of <100>-oriented CdTe bulk in detail, which is dominated by the martensitic transformation. The stress follows Hooke's law in the strain range of 0% to 7%, and its slope represents Young's modulus of 20.6 GPa in the <100> direction of CdTe. When the strain exceeds 8%, the stress increases nonlinearly and smoothly with strain. That is because after exceeding the elastic limit in the <100> direction of CdTe (about 1.4 GPa), the BCC-Cd phase begins to nucleate uniformly in the unstable local region of the FCC-Cd matrix, as shown in Figure 2e–B. It is worth noting that, compared with the standard BCC structure, the BCC-Cd phase formed in the early stage has a relatively large *c*-axis. This is equivalent to the BCC-Cd phase under the *c*-axis tensile strain because it comes from

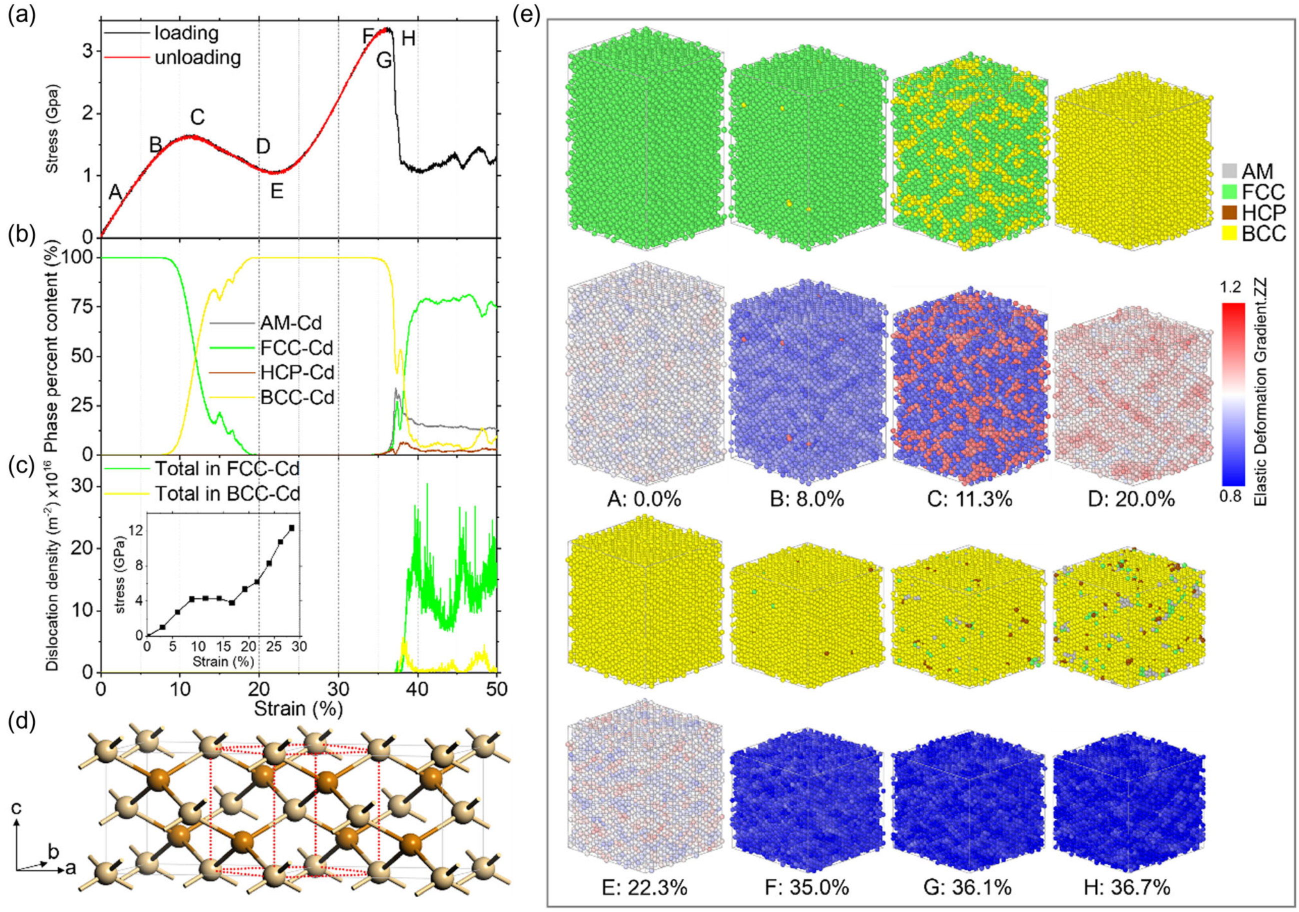

Figure 2. Deformation behavior of <100>-oriented CdTe bulk during compression at 300 K: a) stress–strain curves during compressive loading and unloading; b) evolution of phase content with strain during compression; c) evolution of total dislocation density with strain during compression; The inset illustrates the results of QM-MD simulations of a 32-atom CdTe model, successfully replicating the non-linear stress-strain relationship; d) β-tin-like CdTe generated from c-axis compressed ZB-CdTe, in which the lattice parameters are $a = b = 7.4$ Å and $c = 5.23$ Å. Red dotted lines show the unit cell of β-tin-like CdTe with a space group of $I\text{-}4\,m2$, in which the lattice parameters are $a = b = c = 5.23$ Å. Cd-sublattice here can be easily identified as a BCC structure; The Cd and Te atoms are represented by light yellow and brown balls, respectively. e) Evolution of atomic configuration and distribution of elastic deformation gradient.ZZ with strain during compression. The numerical value of the elastic deformation gradient represents the deformation ratio relative to the ideal structure.

compressing FCC-Cd through Bain transformation.[28] The strain distribution of the elastic deformation gradient.ZZ[29] shows that the tensile state is completely consistent with the phase composition (Figure 2e–B, C). Therefore, the transformation to BCC-Cd in the tensile state slows the increase in compressive stress and leads to nonlinear behavior.

The nucleated BCC-Cd regions continuously grow with increasing strain, resulting in a sustained slowing of the increase in compressive stress. At 11.3% strain, the stress reaches the first maximum and starts to decrease with increasing strain (Figure 2e–C). The BCC-Cd regions continue to grow until the phase transformation is completed at 20% strain (Figure 2e–D). This clear observation of nucleation and growth from 8% to 20% strain indicates that the process is indeed a martensitic phase transition rather than a mere compressive deformation. The BCC-Cd is still in a tensile state at 20% strain, leading to a further stress decrease. The BCC-Cd reaches the standard lattice with c/a of 1 when the strain increases to 22.3% (Figure 2e–E). However, this newly discovered CdTe phase completely transforms back to ZB-CdTe structure after unloading to zero, indicating that it is a constrained crystal structure and cannot be retained at ambient pressure. This is akin to the existence of "compressed graphite" with a 3.1 Å interlayer spacing, which is attributed to the confinement of gradia interfacial structures[30] or a pressure environment of approximately 5 GPa.[31] Therefore, in the experiments, while we observed unique stress–strain curves, it was challenging to find any traces of structural changes in the samples after unloading. Furthermore, to corroborate our findings, we conducted QM-MD simulations of a 32-atom CdTe model in the <100> orientation at 300 K, successfully replicating the non-linear stress–strain relationship as shown in the inset of Figure 2c. Despite the differences in detail between the two simulations, attributed mainly to the significant disparity in the number of atoms used, the consistency of the results sufficiently validates the presence of hyper-elastic deformation we observed and underscores the high accuracy of the ML-FF used in our study.

After reaching a strain of 22.3%, the material transitions into uniaxial compression of the newly formed structure. Initially, it exhibits a linear response phase, from which we can determine a Young's modulus of 22.6 GPa. As the strain increases to 35%, the stress deviates from linear increase due to the local instability in the structure caused by extreme compression. It can be proved by the sporadic appearance of local amorphous (AM), FCC, and HCP atoms and the corresponding strain distribution (Figure 2e–F). The stress reaches the maximum at the strain of 36.1%, which corresponds to the limit of hyper-elastic compression along <100>-oriented CdTe. At this point, the nuclei of other phases begin to grow (Figure 2–G). Then, the stress starts to decrease with the strain, probably due to the release of some compressive stress caused by the growth of other phases (Figure 2e–H). Overall, the deformation mechanism of <100>-oriented CdTe under uniaxial compression is dominated by martensite transformation, leading to hyper-elastic deformation with an extra-large elastic strain capacity of 36%. It is important to note that differences in strain rates and sample conditions between MD simulations and experiments make it impossible to exactly replicate the experimental stress–strain curves. However, the hyper-elastic deformation mechanism provided by MD simulations clearly explains the abnormal deformation behavior observed in experiments under compression along the <100> direction.

The drastic drop in stress after 36.7% strain indicates the failure stage, which is caused by the formation of an amorphous shear band within the BCC-Cd under resolved shear stress (**Figure** 3d–I). The stress release promotes the reverse martensitic transformation from BCC- to FCC-Cd. At a strain of 37.2% and 37.6%, the initial nucleation of dislocations in the FCC- and BCC-Cd occurs, respectively (Figure 3d–I, J). Due to the lack of defects before the phase transformation, dislocation nucleation is unfavorable, while the interface or amorphous structure formed after the phase transformation can act as both sources and absorbers of dislocations. Dislocation nucleation and motion cause relatively smooth plastic deformation compared to the discontinuous deformation caused by shear amorphization, resulting in gentle stress changes with strain from 37.2% to 37.6%. Then, the stress showed a rapid decrease again due to the reduction of dislocation density with strain from 37.6% to 37.9%. The diffuse distribution of BCC, FCC, and amorphous phases at this stage leads to the formation of many phase interfaces, which act as absorption sources for dislocations. The high number of dislocations escaping to these interfaces results in "dislocation starvation"[32] within the crystals, reducing the density of movable dislocations and making the plastic flow difficult with strain from 37.6% to 37.9%. However, the limited dislocation movement promotes atomic diffusion, and the amorphous structure recrystallizes to BCC structure. At the strain of 37.9%, the BCC reaches the local maximum content, and the dislocation density in BCC also reaches the maximum (Figure 3d–K). The nearly integrated BCC phase provides favorable conditions for dislocation movement, leading to dislocation-dominate plastic deformation. Therefore, the added stress is released through dislocation-dominated plastic deformation with a strain beyond 37.9%, which keeps the total stress in a stable range. Moreover, the movement of dislocations with Burgers vectors of $a1/2<111>$ makes the unstable BCC phase transform back to the stable FCC phase through a reverse martensitic transformation in Kurdjumov–Sachs (KS)

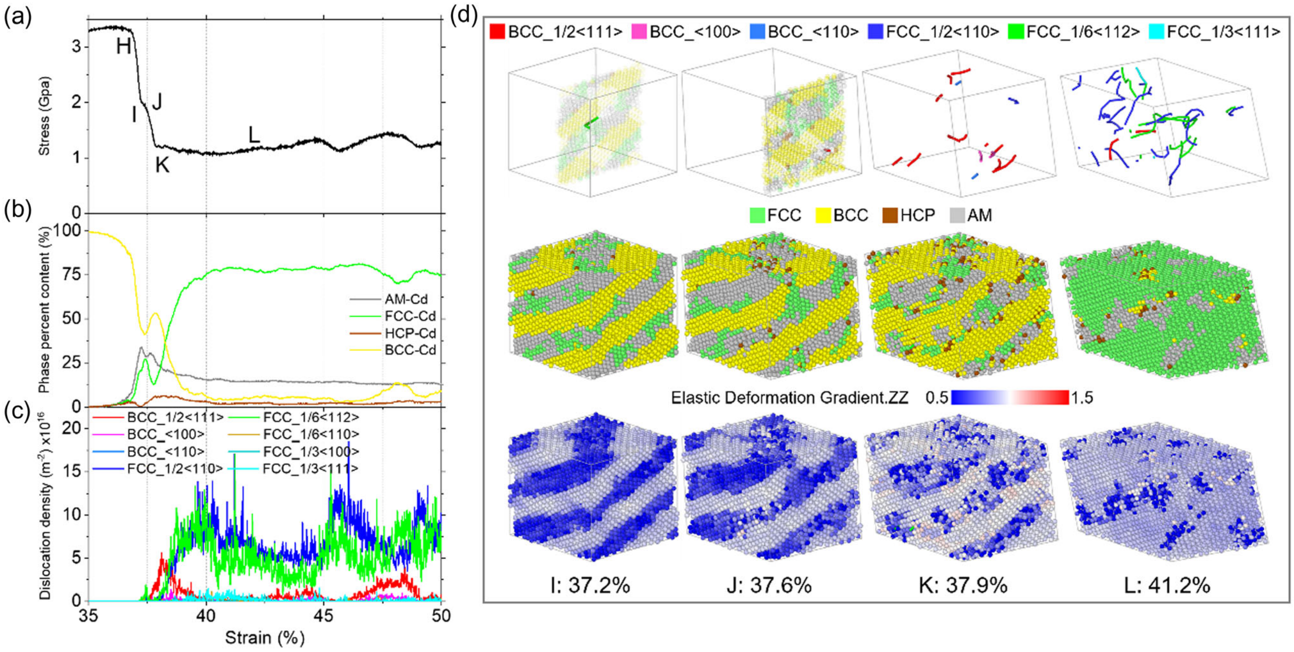

Figure 3. Deformation behavior of <100>-oriented CdTe bulk after a failure during compression at 300 K: a) Stress–strain curves with strain beyond 35%; b) evolution of phase content with strain beyond 35%; c) evolution of dislocation density in BCC- and FCC-Cd structure with strain beyond 35%; d) evolution of atomic configuration and dislocations, and distribution of elastic deformation gradient.ZZ with strain beyond 35%.

models[28,33,34] (Figure 3d–L). Therefore, the plastic deformation beyond 41.2% was dominated by dislocation movement in the FCC phase. Based on the aforementioned analysis, the <100>-oriented CdTe bulk exhibits brittle failure characteristics during compression deformation due to "dislocation starvation". The polycrystalline structures formed after failure show excellent dislocation-dominated plastic deformation properties because the phase interfaces provided sufficient dislocation density.

2.3. Deformation Mechanism along <110>-Oriented CdTe Bulk

The evolution of stress, structure, and dislocation during the compression deformation of the <110>-oriented CdTe bulk are shown in **Figure 4**. From the stress–strain curve in Figure 4a, the compression process consists of four stages: 1) initial linear response stage within the strain of 12.8%; 2) discontinuous descent stage of stress within the strain between 12.8% and 15.5%; 3) another linear response stage within the strain between 15.5% and 20.8%; 4) load drop stage, i.e., failure stage, with strain beyond 20.8%. A competitive relationship also exists between phase transformation and dislocation motion at different stages during the compression deformation of the <110>-oriented CdTe bulk (Figure 4a–c). The loading and unloading curves within the strain of 20.8% almost overlap with each other, except for the intermediate nonlinear stage, indicating that the nonlinear response stage belongs to hyper-elastic deformation, and there is another martensitic transformation different from that in the compression deformation of the <100>-oriented CdTe bulk.

The atomic configuration during compression deformation of the <110>-oriented CdTe bulk is presented in Figure 4d. Within the strain of 12.8%, There is no phase transformation, which corresponds to linear elastic deformation, and the Young's modulus in the <110> direction of CdTe is 37.6 GPa. The stress abruptly drops when the strain exceeds 13%, which may be mistaken for a structural failure. Figure 4d–B shows that the local instability region in the FCC matrix transits into a BCC structure through shear. The lattice shear along the <110> direction of FCC indicates that martensitic transformation mainly occurs through the KS model.[28,33,34] The HCP phase produced from the shear of FCC also supports this shear transformation mode.[35] Unlike the continuous lattice distortion in the Bain model, this shear transformation mode leads to the rapid nucleation and growth of BCC along the shear plane, resulting in a "jump/discontinuity" of stress (Figure 4d–B). The BCC phase gradually grows with strain, and the phase

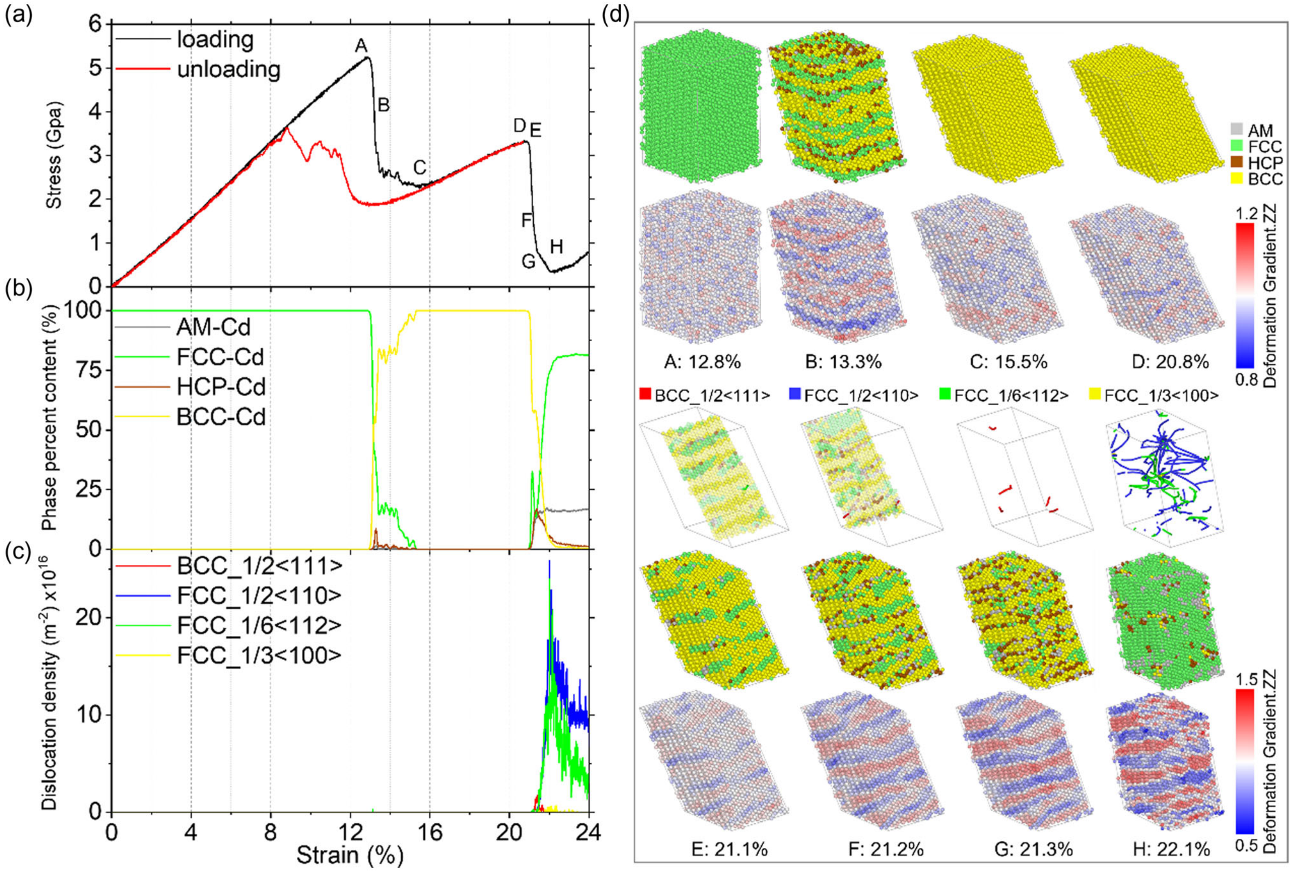

Figure 4. Deformation behavior of <110>-oriented CdTe bulk during compression loading at 300 K: a) stress–strain curves during compression loading and unloading; b) evolution of phase content with strain during compression loading; c) evolution of dislocation density in BCC- and FCC-Cd structure with strain during compression loading; d) evolution of atomic configuration and dislocations, and distribution of deformation gradient.ZZ with strain during compression loading.

transformation is complete at 15.5% (Figure 4d–C). Therefore, the deformation of the BCC structure becomes elastic within the strain from 15.5% to 20.8% (Figure 4d–D). However, the unstable BCC structure could easily transit into the FCC structure via the reverse martensitic transformation when the strain exceeds the elastic limit, leading to a sudden decrease in stress (Figure 4d–E). Similarly, the interface generated by this local phase transformation promotes the nucleation of dislocations (Figure 4d–E–G). However, due to the "dislocation starvation" at the initial stage, the density of movable dislocations left in the crystal is relatively small, making plastic flow challenging within the strain from 21.1% to 21.3%. As the strain increases, dislocation motion gradually dominates the plastic deformation process (Figure 4d–H), the same as the plastic deformation of the <100>-oriented CdTe bulk. The <110>-oriented CdTe bulk shows brittle failure characteristics during compression deformation due to the "dislocation starvation". However, the failure is caused by shear transformation from BCC to FCC instead of the amorphous phase. The martensitic transformation prefers the KS model with shear deformation to the Bain model during compression along the <110> direction.[28] Therefore, the reverse martensitic transformation that causes failure is also the KS model with shear deformation. This shear-induced martensitic transformation appears not to have been observed in aforementioned experiments, possibly because the BCC phase formed by this shear deformation requires a specific shear strain environment to stabilize, which is challenging to achieve in the micropillar samples used in the experiments.

2.4. Deformation Mechanism along <111>-Oriented CdTe Bulk

The evolution of stress, structure, and dislocation during the compression deformation of the <111>-oriented CdTe bulk is shown in **Figure 5**. From the stress-strain curve in Figure 5a, the compression process consists of three stages: 1) initial linear response stage within the strain of 7%; 2) continuous but nonlinear response stage within the strain between 7% and 16.9%; 3) load drop stage, i.e., failure stage, with strain beyond 16.9%. Like the deformation behavior of the other two-oriented CdTe bulk, there is also a competitive relationship between phase transformation and dislocation motion at different stages during the compression deformation of the <111>-oriented CdTe bulk (Figure 5a–c). Young's modulus calculated from the initial linear response stage is 46.9 GPa in the <111> direction of CdTe.

The structural analysis revealed that the local region of the CdTe structure begins to exhibit distortions causing atoms to deviate from their equilibrium positions after surpassing the elastic strain limit of 7%, leading to a nonlinear increase in stress with strain, as shown in Figure 5d–A. Specifically, along the {111} planes, the kinked CdTe bilayers in a diamond-like structure transform into nearly a single plane layer, which should be attributed to the ultra-high rate of compressive deformation in MD simulations. Since <111> orientation is not the <100> orientation required by the Bain model but is also perpendicular to the (111) shear plane required by the shear model,[28] no

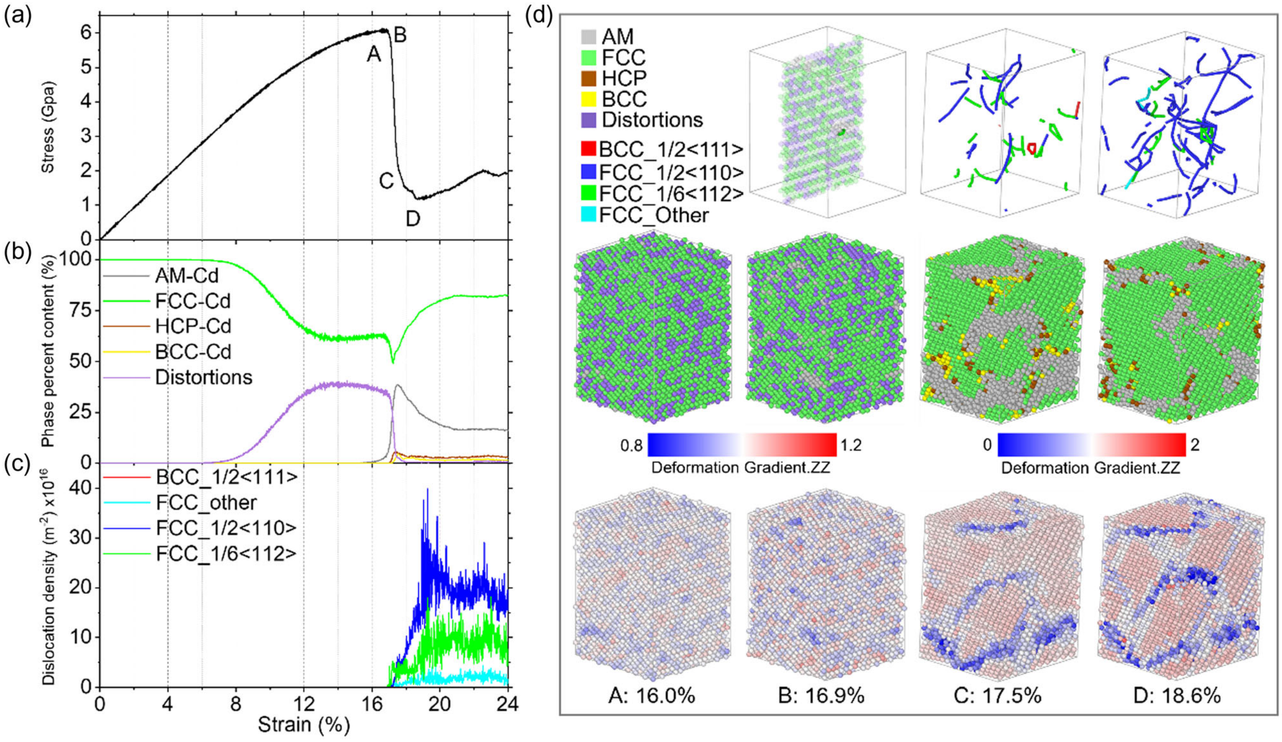

Figure 5. Deformation behavior of <111>-oriented CdTe bulk during compression loading at 300 K: a) stress–strain curves during compression loading and unloading; b) evolution of phase content with strain during compression loading; c) evolution of dislocation density in BCC- and FCC-Cd structure with strain during compression loading; d) evolution of atomic configuration and dislocations, and distribution of deformation gradient.ZZ with strain during compression loading.

martensitic transformation from FCC to BCC was observed here. In addition, the transformation from the distortion region to an amorphous phase occurs after the strain exceeds 15%, indicating that the distortion is extremely unstable (Figure 5d–B). This localized amorphous phase provides the phase interface as the dislocation source, so dislocation nucleation appears in FCC when the strain increases to 16.9%, breaking the equilibrium of the structure and causing the material to fail. As discussed earlier, the diffusely distributed FCC structure leads to "dislocation starvation", so plastic flow is difficult with strain from 16.9% to 17.5%. Therefore, it is the structural amorphization that dominates the brittle failure with strain from 16.9% to 17.5%. There is no obvious shear deformation in the lattice (Figure 5d–C) because it is not easy to form obvious shear bands in a polycrystalline state before failure, but the growth of the local amorphous region. Furthermore, the amorphous growth aggregated the originally dispersed FCC to alleviate the "dislocation starvation". When the strain reached 17.5%, dislocation motion became dominant in plastic deformation, and the stress curves began to flatten out (Figure 5d–C). The dislocation movement promotes atomic diffusion, and recrystallization occurs from amorphous to FCC with strain (Figure 5d–D). So, dislocation motion dominates the plastic deformation of <111>-oriented CdTe bulk with strain beyond 17.5%, like the plastic deformation of the previous two oriented CdTe bulk. Unlike the other two orientations, the failure of <111>-oriented CdTe bulk is caused by dislocation nucleation rather than reverse martensitic transformation. But it also exhibited brittle failure characteristics, resulting from plastic flow difficulties caused by the initial "dislocation starvation". The dislocation motion of <111>-oriented CdTe bulk occurs earlier because there is no unstable phase BCC present. The <111> orientation does not favor the formation of the BCC phase during uniaxial compression due to the lack of a suitable phase transition path.[28] So, there is no hyper-elastic deformation caused by martensitic transformation during the compression deformation of the <111>-oriented CdTe bulk.

2.5. Simulated Orientation-Dependent Nanopillar Responses

To simulate the micropillar compression experiments more accurately, we conducted compression simulations of the CdTe pillar with three different orientations, as shown in **Figure 6**. The stress–strain curves reveal that only <100>-oriented CdTe pillar exhibits hyper-elastic deformation, while the other two other pillars do not. The evolution of phase content shows that only the <100>-oriented CdTe pillar undergoes a martensitic transformation during compression, akin to what is observed in bulk compression. Both simulation calculations resulted in hyper-elastic deformation caused by martensitic phase transformation, suggesting that the atomic mechanism behind the unique deformation behavior observed experimentally in the [100] direction is likely to be of this nature. In contrast, the other two orientations undergo partial amorphization, a result of the formation of a shear band upon exceeding the elastic deformation limit. Comparing the dislocation evolution and

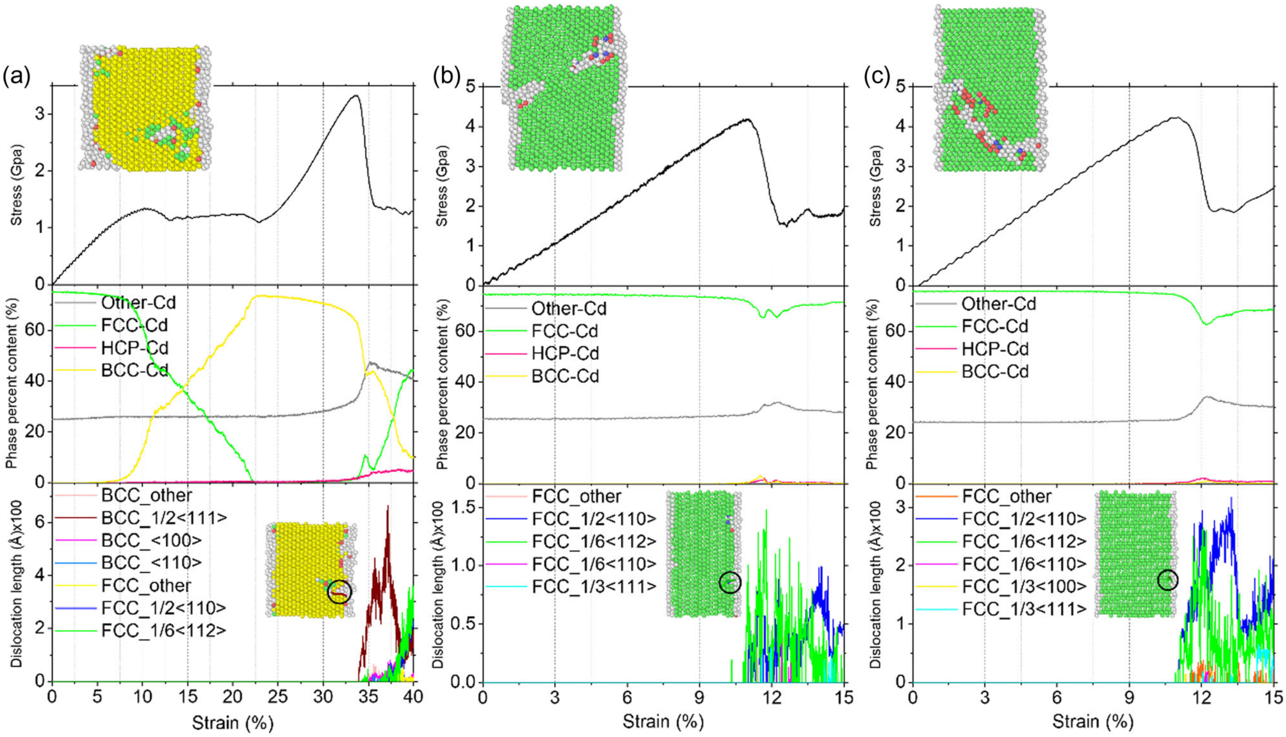

Figure 6. Deformation behavior of a) <100>, b) <110>, and c) <111>-oriented CdTe pillar during compression loading at 300 K: (Upper) stress–strain curves during compression loading; The insets show the atomic configuration after failure. (Middle) Evolution of phase content with strain during compression loading; (Below) evolution of dislocation length with strain during compression loading; the insets show that the initial nucleation positions of dislocations are all on the surface.

stress-strain curve of the <110> and <111>-oriented CdTe pillars, it is clear that dislocation nucleation occurs before failure. A significant plastic deformation stage is achieved due to dislocation movement before failure in the <110> and <111>-oriented CdTe pillars, while it is absent in <100>-oriented CdTe pillar because the nucleation of dislocations triggers the reverse martensitic transformation from unstable BCC to FCC (Figure 6a). Therefore, under the combined influence of phase transition and dislocation movement, the stress of <100>-oriented CdTe pillar decreases more rapidly after exceeding the elastic limit (Figure 6a). Additionally, the inset in Figure 6 shows that the initial nucleation of dislocations always originates from the surface. Notably, the dislocations with Burgers vectors of $a1/6 < 112>$ always nucleate first in both bulk and pillars, likely due to their lowest energy.[22] The surface acting as the dislocation source makes the dislocation play a dominant role in the deformation mechanism of the pillar relative to bulk, resulting in a smaller failure strain of the <110> and <111>-oriented CdTe pillars compared to their bulk counterparts.

Overall, the failure mechanism in bulk CdTe is predominantly triggered by phase transformation, followed by the emergence of amorphous shear bands and dislocations. This sequence is largely due to the difficulty in generating dislocation sources within the single crystal structure before failure, compelling the material to undergo phase transformation as a primary failure trigger. In contrast, the pillars, having surfaces that serve as dislocation sources, invariably experience failure initiated by dislocation activities. This distinction highlights the critical role of surface-induced dislocations in determining the failure mechanisms of micro-scaled materials as opposed to their bulk counterparts. During compression in the <100> direction, the deformation direction of the martensitic transformation following the Bain path is also along the <100> direction. Moreover, the lower triggering stress for the phase transition (approximately 1.4 GPa) makes the transformation more likely to occur, thus phase transition predominates in both bulk and pillar deformation mechanisms of <100>-oriented CdTe. Consequently, the <100>-oriented CdTe can sustainably accommodate over 34% elastic strain due to hyper-elastic deformation.

3. Conclusion

In summary, we studied the deformation behavior of CdTe bulk and pillar with <100>, <110>, and <111> orientations under uniaxial compression using ML-FF based MD simulations and in-situ SEM micro-pillar compression tests. Unlike classical interatomic potential, our ML-FF MD revealed the complex competition between martensitic transformation and dislocation motion in CdTe deformation, offering insights that align with current experimental observations. In the CdTe bulk, martensitic transformation dominates, and dislocation nucleation is significantly inhibited due to the lack of dislocation sources. In contrast, in the CdTe pillar, deformation behavior is dominated by dislocation nucleation and movement, which are enabled by the presence of a surface as dislocation source.

Our study found that only the <100>-oriented CdTe bulk and pillar can stably possess more than 34% elastic strain due to hyper-elastic deformation caused by stable martensitic transformation. Additionally, <111>-oriented CdTe bulk and pillar possess maximum compressive strength. Therefore, the <100>-oriented CdTe is suitable for enduring large deformations, whereas the <111>-oriented CdTe is more apt for withstanding high stresses, an aspect crucial for the design and application of flexible devices in the future.

The data that support the findings of this study are available from the corresponding author upon reasonable request.

4. Experimental Section

CdTe Single Crystals Preparation: The CdTe single crystal was purchased from the MTI Corporation with <100>, <110>, and <111> orientation, respectively. The surface was polished with a roughness less than 1.5 nm. The CdTe crystal size is 5 × 5 × 1 mm. The orientation of the crystal was confirmed using the Rigaku Smart Lab X-ray diffractometer.

Experimental Measured Mechanical Responses: The tested samples were fabricated into micro-pillars using a focused ion beam (ThermoFisher Scientific Scios 2 Dual-Beam) with a Ga^+ ion beam working voltage of 30 kV. The initial beam current was selected as 15 nA to rapidly remove the material, and then reduced to 0.1 nA for final polishing of the micro-pillar to minimize the surface damage. To ensure the nanopillar remained a single crystal, the FIB beam was vertical to the polished surface. The diameters of the micro-pillars were approximately 10.5 μm with a height-to-diameter ratio of 2–3. At least three micro-pillars were tested in each experiment. Additionally, nano-indentation was conducted to obtain a load–displacement curve for single crystals along different orientations using an Agilent Technologies Nano Indenter G200 equipped with a Berkovich diamond indenter. The mechanical responses of high-quality single crystal were evaluated using an in-situ SEM compression test (Hysitron PI88 PicoIndentor) with displacement control and a constant strain rate of $2 \times 10^{-3}\ s^{-1}$.

MD Simulations Using ML-FF: All MD simulations were performed using the large-scale atomic/molecular massively parallel simulator (LAMMPS). The atomistic interactions of CdTe were described using the accurate ML-FF,[22] in which the interactions of atoms with their neighbors are represented by a deep neural network. The neural network parameters were developed using the DeePMD-kit package by training the system energy, atomic force, and virial stress obtained from extensive DFT simulations.[36] This ML-FF has been successfully applied to the MD study of the structural evolution of dislocations in CdTe, which demonstrates its accuracy and robustness.[22] The velocity Verlet algorithm was used for integrating the equations of motion with a timestep of 1.0 fs in all MD simulations. Periodic boundary conditions were applied in all three directions. At the beginning of each simulation, the atomic system was fully relaxed using the conjugate gradient algorithm. Isobaric-isothermic (NPT) ensemble (constant pressure, constant temperature, and constant number of atoms) molecular dynamics at ambient conditions ($T = 300$ K and $P = 1$ bar) was performed for 50 ps to ensure that the system attains the equilibrium density, followed by canonical (NVT) ensemble dynamics at 300 K for an additional 50 ps until the total energy converged. A Nosé–Hoover temperature thermostat and Nosé–Hoover pressure barostat were applied throughout the simulation, with damping constants of 0.1 and 1.0 ps for the thermostat and barostat, respectively. During compression deformation, the NPT ensemble was employed in all dimensions (except z-dimension) to maintain zero lateral pressure (i.e., constant uniaxial strain rate). The systems were deformed at 300 K with a high strain rate of $10^9\ s^{-1}$.

All atom visualizations were obtained using OVITO,[37] while the polyhedral template matching (PTM)[29] and dislocation extraction algorithm (DXA)[38] were used to analyze the phase transformation and dislocation evolutions under deformation, respectively. In the PTM analyses, the local packing around each atom was fitted to three templates (fcc, bcc, and hcp), and the outcome of which was evaluated by the root-mean-square deviation (RMSD) from these templates. The local packing was then identified as the template that produced the lowest RMSD. If all RMSD values exceeded a pre-assigned RMSD cut-off (set as 0.15 in this study), the local packing of an atom was identified as "unknown", i.e., amorphous (AM). The DXA method was employed to confirm whether plastic deformation occurred during the compression loading process, and it can identify all the dislocation defects in the crystal. In addition, the deformation gradient of systems obtained from PTM and atomic strain modifier were used to analyze the local strain under deformation. The elastic deformation gradient tensor was calculated locally at each atom in the system by taking into account the correspondences between the actual atomic positions and the positions of the ideal structure.[29]

QM-MD Simulations: We utilized quantum mechanics (QM) MD simulations for a 32-atom CdTe model under compression to validate the ML-FF MD results. The Vienna Ab initio Simulation Package (VASP) with a plane-wave basis set and the Perdew–Burke–Ernzerhof (PBE) functional for solids (PBEsol) were employed for these simulations.[39,40] Key parameters included a 300 eV energy cutoff for plane-wave expansion and a 1.0×10^{-6} eV energy convergence criterion. The first Brillouin zone was sampled at the Γ-point, and Gaussian smearing with a width of 0.05 eV was used for electron occupancy. The atomic system was initially relaxed using the NPT ensemble at 300 K, with temperature and pressure controlled by the Langevin thermostat[41] and the Parrinello–Rahman barostat,[42] respectively. The compression simulations were conducted with a step size of 0.03/step, and at each step, the NVT ensemble with 600 fs was implemented for fixed volume simulations at 300 K, using the Langevin thermostat. Additionally, a timestep of 3.0 fs was applied for integrating the equations of motion in all QM-MD simulations.

Acknowledgements

This work is supported by the US National Science Foundation (grant no. CMMI-2019459/2330728). This work used Anvil at Purdue University through allocation MCH220024 from the Advanced Cyberinfrastructure Coordination Ecosystem: Services & Support (ACCESS) program, which is supported by National Science Foundation grant #2019459.

Conflict of Interest

The authors declare no conflict of interest.

Data Availability Statement

The data that support the findings of this study are available from the corresponding author upon reasonable request.

Keywords

cadmium telluride, deformation mechanism, machine-learning force, martensitic transformation, molecular dynamics

Received: December 5, 2023
Revised: March 30, 2024
Published online: April 12, 2024

---

[1] S. Kim, H. Van Quy, C. W. Bark, *Mater. Today Energy* **2021**, *19*, 100583.
[2] B. V. Rajendra, D. Kekuda, *J. Mater. Sci. Mater. Electron.* **2012**, *23*, 1805.
[3] R. L. Rowlands, V. Barrioz, E. W. Jones, S. J. C. Irvine, D. A. Lamb, *J. Mater. Sci. Mater. Electron.* **2008**, *19*, 639.
[4] J. Ramanujam, D. M. Bishop, T. K. Todorov, O. Gunawan, J. Rath, R. Nekovei, E. Artegiani, A. Romeo, *Prog. Mater. Sci.* **2020**, *110*, 100619.
[5] R. Balasubramanian, W. R. Wilcox, *Mater. Sci. Eng. B* **1993**, *16*, 1.
[6] E. Y. Gutmanas, N. Travitzky, U. Plitt, P. Haasen, *Scr. Metall.* **1979**, *13*, 293.
[7] K. Nakagawa, K. Maeda, S. Takeuchi, *J. Phys. Soc. Jpn.* **1980**, *49*, 1909.
[8] K. Guergouri, N. Brihi, R. Triboulet, *J. Cryst. Growth* **2000**, *209*, 709.
[9] K. Guergouri, N. Brihi, Y. Marfaing, R. Triboulet, *J. Cryst. Growth* **2003**, *256*, 230.
[10] M. Nagabhooshanam, V. H. Babu, *J. Mater. Sci.* **1985**, *20*, 4329.
[11] J. Li, Q. An, *Int. J. Mech. Sci.* **2023**, *242*, 107998.
[12] J. Li, Q. An, *J. Eur. Ceram. Soc.* **2023**, *43*, 208.
[13] Z. Zhang, X. Zhang, X. Guo, F. Ye, Y. Huo, *Scr. Mater.* **2013**, *69*, 457.
[14] Z. Zhang, B. Wang, X. Zhang, *Scr. Mater.* **2014**, *72–73*, 39.
[15] Z. Zhang, N. Duan, B. Wang, Y. Huo, B. Zhang, X. Zhang, F. Ye, *Scr. Mater.* **2014**, *93*, 12.
[16] Q. Xiang, X. Peng, H. Yang, H. Xiang, C. Huang, B. Yang, X. Yue, T. Fu, *Ceram. Int.* **2017**, *43*, 14405.
[17] M. A. M. Munshi, S. Majumder, M. Motalab, S. Saha, *Mater. Res. Express* **2019**, *6*, 105083.
[18] D. K. Ward, X. W. Zhou, B. M. Wong, F. P. Doty, J. A. Zimmerman, *J. Chem. Phys.* **2011**, *134*, 244703.
[19] J. S. Smith, O. Isayev, A. E. Roitberg, *Chem. Sci.* **2017**, *8*, 3192.
[20] P. Rowe, G. Csányi, D. Alfè, A. Michaelides, *Phys. Rev. B* **2018**, *97*, 054303.
[21] D. Marchand, A. Jain, A. Glensk, W. A. Curtin, *Phys. Rev. Mater.* **2020**, *4*, 103601.
[22] J. Li, K. Luo, Q. An, *Int. J. Plast.* **2023**, *163*, 103552.
[23] Y.-L. Li, *Solid State Commun.* **2013**, *155*, 73.
[24] C. Xu, W. Zhang, M. Hu, J. Zhang, Z. Lang, P. Li, H. Liu, P. Wang, C. Liu, *Appl. Phys. A* **2022**, *128*, 728.
[25] S. Zhang, Z. Li, K. Luo, J. He, Y. Gao, A. V. Soldatov, V. Benavides, K. Shi, A. Nie, B. Zhang, W. Hu, M. Ma, Y. Liu, B. Wen, G. Gao, B. Liu, Y. Zhang, Y. Shu, D. Yu, X.-F. Zhou, Z. Zhao, B. Xu, L. Su, G. Yang, O. P. Chernogorova, Y. Tian, *Natl. Sci. Rev.* **2022**, *9*, 527.
[26] A. Ojha, H. Sehitoglu, *Int. J. Plast.* **2016**, *86*, 93.
[27] S. Alptekin, *J. Mol. Model.* **2013**, *19*, 421.
[28] L. Sandoval, H. M. Urbassek, P. Entel, *New J. Phys.* **2009**, *11*, 103027.
[29] P. M. Larsen, S. Schmidt, J. Schiøtz, *Modell. Simul. Mater. Sci. Eng.* **2016**, *24*, 055007.
[30] K. Luo, B. Liu, W. Hu, X. Dong, Y. Wang, Q. Huang, Y. Gao, L. Sun, Z. Zhao, Y. Wu, Y. Zhang, M. Ma, X.-F. Zhou, J. He, D. Yu, Z. Liu, B. Xu, Y. Tian, *Nature* **2022**, *607*, 486.
[31] F. P. Bundy, J. S. Kasper, *J. Chem. Phys.* **1967**, *46*, 3437.
[32] J. R. Greer, W. D. Nix, *Phys. Rev. B* **2006**, *73*, 245410.
[33] A. V. Korchuganov, A. N. Tyumentsev, K. P. Zolnikov, I. Y. Litovchenko, D. S. Kryzhevich, E. Gutmanas, S. Li, Z. Wang, S. G. Psakhie, *J. Mater. Sci. Technol.* **2019**, *35*, 201.
[34] S. Karewar, J. Sietsma, M. J. Santofimia, *Acta Mater.* **2018**, *142*, 71.
[35] H. Zhang, B. Wei, X. Ou, S. Ni, H. Yan, M. Song, *Int. J. Plast.* **2022**, *156*, 103357.
[36] H. Wang, L. Zhang, J. Han, W. E, *Comput. Phys. Commun.* **2018**, *228*, 178.
[37] A. Stukowski, *Modell. Simul. Mater. Sci. Eng.* **2010**, *18*, 015012.
[38] A. Stukowski, V. V. Bulatov, A. Arsenlis, *Modell. Simul. Mater. Sci. Eng.* **2012**, *20*, 085007.
[39] G. Kresse, J. Furthmüller, *Phys. Rev. B* **1996**, *54*, 11169.
[40] J. P. Perdew, A. Ruzsinszky, G. I. Csonka, O. A. Vydrov, G. E. Scuseria, L. A. Constantin, X. Zhou, K. Burke, *Phys. Rev. Lett.* **2008**, *100*, 136406.
[41] M. P. Allen, D. J. Tildesley, *Computer Simulation Of Liquids*, Oxford University Press, Oxford, United Kingdom **2017**.
[42] R. Martoňák, A. Laio, M. Parrinello, *Phys. Rev. Lett.* **2003**, *90*, 075503.